Supplementary Information for

Engineering conductive network of atomically thin bismuthene with rich defects enables CO_2 reduction to formate with industry-compatible current densities and stability

Min Zhang,[a,c] Wenbo Wei,[a,c] Shenghua Zhou,[a,c] Dong-Dong Ma,[a] Aihui Cao,[a,c] Xin-Tao Wu,[a,b,c] Qi-Long Zhu*[a,b,c]

[a] State Key Laboratory of Structural Chemistry, Fujian Institute of Research on the Structure of Matter, Chinese Academy of Sciences (CAS), Fuzhou 350002, China

[b] Fujian Science & Technology Innovation Laboratory for Optoelectronic Information of China, Fuzhou 350108, China

[c] University of Chinese Academy of Sciences, Beijing 100049, China

*E-mail: qlzhu@fjirsm.ac.cn

1. **Experimental details**

1.1 Chemicals

GO dispersion solution (5.88 mg mL^{-1}) was purchased from Shandong Yuhuang New Energy Technology Co., Ltd. Bismuth nitrate pentahydrate ($Bi(NO_3)_3 \cdot 5H_2O$), nitric acid (65~68%, HNO_3), hexadecyltrimethylammonium bromide (CTAB), potassium bicarbonate ($KHCO_3$), potassium hydroxide (KOH), Phenolphthalein, N,N-dimethylformamide (DMF), and ethanol were obtained from Sinopharm Chemical Reagent Co. Ltd. (Shanghai, China). Bismuth power was purchased from Energy Chemical Reagent Co. Ltd. (Shanghai, China). Nafion solution (5 wt%) was obtained from Sigma-Aldrich. All chemical reagents were used directly without further purification.

1.2 Instrumentation

Powder X-ray diffraction (PXRD) patterns were measured by the Miniflex600 X-ray diffractometer at 40 kV and 40 mA with Cu Kα radiation. The morphologies of the samples were observed by field-emission scanning electron microscopy (FESEM, JSM6700, operated at an accelerating voltage of 5 kV) and transmission electron microscopy (TEM, F20, operated at an accelerating voltage of 200 kV). AFM images were obtained in a Bruker Dimension ICON atomic force microscope. The Fourier transform infrared (FTIR) spectra were recorded on a Spectrum One Fourier transform infrared spectrometer (Perking-Elmer Instruments) by using the KBr as a background. X-ray photoelectron spectroscopy (XPS) with monochromatized Al Kα X-rays (hν = 1486.6 eV) radiation (ThermoFisher Scientifc Co. ESCALAB 250Xi, USA) was used to investigate the surface electronic properties. The binding energy calibration of the spectra was referred to the C1s peak located at BE = 284.8 eV for the analysis. Operando attenuated total reflection-infrared (ATR-IR) spectra were recorded on the NICOLET 6700 instrument.

1.3 Preparation

*Preparation of **GO paper**:* The aqueous GO dispersion (25 mL) at a concentration of 2 mg mL^{-1} was vacuum filtrated to prepare the GO paper, which was dried at room temperature for the subsequent use.

*Preparation of **Bi_2O_3 networks**:* $Bi(NO_3)_3 \cdot 5H_2O$ (0.987g) was added to DMF (20 mL) during vigorous stirring at room temperature, and then the **GO paper** was immersed in the solution of $Bi(NO_3)_3 \cdot 5H_2O$ (0.1 mol L^{-1}) for 24 h. After immersion, the GO paper was taken out and washed by DMF twice and dried at 150 °C for 12 h in vacuum oven. Finally, the hybrid GO paper was treated sequentially at 350 °C for 2 h and at 500 °C for 1 h in air to burn out GO with a heating rate of 5 °C min^{-1}.

*Preparation of **Bi-ene-NW***: Bi-ene-NW was synthesized via an in situ electrochemical transformation approach from the obtained Bi_2O_3 network in a two-electrode system. The Bi_2O_3 network was dispersed in the mixture of water, ethanol and Nafion solution (8:1:1), and casted onto a 0.5×1.0 cm^2 carbon fiber paper with a catalyst areal loading of 1 mg cm^{-2} as the working electrode. The transformation experiment was carried out in H-type cell with two compartments separated by a piece of proton exchange membrane (Nafion 117). The working electrode and the reference electrode (saturated Ag/AgCl) were placed in the cathode compartment, and the counter electrode (Pt mesh) was placed in the anodic compartment. Each compartment contained 0.5 M $KHCO_3$ electrolyte (10 mL). All potentials were converted to the RHE scale (ERHE = ESCE + 0.198 V + 0.0591 V × pH). Cyclic voltammetry (CV) was performed at a scan rate of 100 mV s^{-1} between 0.376 and 1.176 V (vs. RHE) for 100 cycles in CO_2-saturated 0.5 M $KHCO_3$ electrolyte for the cathodic transformation of the Bi_2O_3 network, generating to Bi-ene-NW (Fig. S6a).

*Preparation of **Bi-NF**:* $Bi(NO_3)_3 \cdot 5H_2O$ (0.243 g) was dissolved into the concentrated HNO_3 (0.125 mL), leading to a transparent solution, which was then added dropwise into deionized water (5 mL) with constant stirring, leading to a solution (Solution A). Concurrently, CTAB (0.125 g) was dissolved into deionized water (60 mL) through ultrasonication to form another transparent solution (Solution B). Then, the solution A was dropwise added into solution B with constant stirring. The mixture was kept at 30 °C for 3 h. The precipitate was collected by centrifugation, completely washed with ethanol and deionized water several times, and dried, which was finally cathodically reduced to the Bi nanoflowers (Bi-NFs), following the similar procedures to Bi-ene-NW.

*Preparation of **Bi-MP**:* The commercial bismuth power was firstly converted into Bi_2O_3 in air at 600 °C for 6 h with a heating rate of 5 °C min^{-1}. Then, the converted Bi_2O_3 was cathodically reduced to the Bi microparticles (Bi-MPs), following the similar procedures to Bi-ene-NW.

Carbon paper supported Bi electrodes were prepared by in situ electrochemical reduction of Bi_2O_3. The obtained electrode was rinsed with water and ethanol immediately, and then tested by PXRD, XPS and SEM. In order to further obtain the detail morphology and nanostructure, these Bi electrodes were placed in ethanol for ultrasonic treatment, and then the ethanol solution containing sample was used immediately for HRTEM and AFM tests. For ATR-IR measurements, firstly, the Bi_2O_3-NS-NW supported on the glassy carbon electrode was electrochemically reduced into Bi-ene-NW. Then, the loaded Bi-ene-NW electrode was used as the working electrode, along with Ag/AgCl as the reference electrode, and platinum wire as the counter electrode.

1.4 Electrochemical measurements

For CO_2RR measurements, the carbon fiber paper supported Bi-ene-NW was directly used as the working electrode in the typical H-type cell with two compartments. The electrolyte was pre-saturated with Ar (pH = 8.4) or CO_2 (pH = 7.4). A constant CO_2 flow of

20 sccm was continuously bubbled into the electrolyte to maintain its saturation during CO_2RR measurements. Cyclic voltammetry and polarization curves were carried out at a scan rate of 10 mV s^{-1}.

In order to analyze the reduction products and calculate their Faradaic efficiency, the electrolysis was performed at selected potentials for 1 h. During the electrolysis, gaseous products were detected by an on-line gas chromatography (GC) (Agilent 7820A) equipped with a molecular sieve 5 Å and two porapak Q columns continuously. The concentration of H_2 and CO was analyzed by a thermal conductivity detector (TCD) and a flame ionization detector (FID), respectively. The quantification of gaseous products was carried out using a conversion factor derived from the standard calibration gases. The Faradaic efficiency of gaseous products was calculated as below:

$$\boldsymbol{FE = \frac{N \times C \times v \times F}{V_m \times j_{total}} \times 100\%} \tag{1}$$

where $\boldsymbol{N}$ is the number of electrons required to form a molecule of product, $\boldsymbol{C}$ is the measured concentration of product, $\boldsymbol{v}$ is the flow rate of CO_2, $\boldsymbol{F}$ is the Faraday constant (96 480 C mol^{-1}), $\boldsymbol{V_m}$ is the molar volume of gas when temperature is 298 K, and $\boldsymbol{j_{total}}$ is the recorded current.

Liquid products were collected at the end of each electrocatalysis and analyzed by 1H NMR (AVANCE III HD). For the NMR, 0.5 ml of the catholyte was mixed with 0.1 ml of D_2O containing dimethylsulfoxide (DMSO, 10 ppm) as the internal standard. The concentration of formate was quantitatively determined from its NMR peak area relative to that of the internal standard using the calibration curve from a series of standard formate solutions. The Faradaic efficiency of formate was calculated as follows:

$$\boldsymbol{FE = \frac{n_{formate} \times N \times F}{Q_{total}} \times 100\%} \tag{2}$$

where $\boldsymbol{n_{formate}}$ is the measured amount of formate in the cathode compartment and $\boldsymbol{Q_{total}}$ is total electric quantity.

The half-cell cathodic energy efficiency (CEE) was calculated as follows:

$$\boldsymbol{CEE = \frac{1.23 - E_{formate}}{1.23 - E_{applied}} \times FE_{formate} \times 100\%} \tag{3}$$

where $\boldsymbol{E_{formate}}$ = –0.2 V vs. RHE is the thermodynamic potential of CO_2 reduction to formate. $\boldsymbol{FE_{formate}}$ is the Faradaic efficiency of formate production. $\boldsymbol{E_{applied}}$ is the applied potential vs. RHE.

Long-term stability test: The stability tests were conducted using the bigger H-cell by adjusting the anolyte and catholyte to 125 mL. In order to avoid the influence of catalyst falling off, the loading amount was change to 2.0 mg cm^{-2}. In the process of electrolysis, CO_2 is continuously converted into formate, and the K^+ ions continuously migrate from anolyte to catholyte through Nafion 117 to maintain the charge balance of electrolyte, which will affect the water oxidation reaction at the anode side and eventually inhibit CO_2 reduction. Therefore, it is necessary to renew the electrolyte after a period of electrolysis.

Flow cell measurements: Flow cell measurements were performed in a custom-designed flow cell reactor. It consisted of Bi_2O_3-loaded GDE (2 mg cm^{-2}, 1×1 cm^2) as the cathode, a piece of anion exchange membrane (Fumapem FAA-3-PK-130) as the separator, and a porous nickel foam as the anode. Ag/AgCl reference electrode with a diameter of 6 mm was located inside the cathode compartment. Electrode potentials were converted to the reversible hydrogen electrode (RHE) scale with 85% iR compensation. During the measurements, CO_2 gas was directly fed to the cathodic GDE at a rate of 20 sccm. The catholyte was 1 M $KHCO_3$ or 1 M KOH. It was forced to continuously circulate through the cathode compartment at a rate of 20 ml min^{-1}.

1.5 Computational methods

DFT calculations were performed using the Vienna ab initio simulation package (VASP) [S15,S16]. The interactions between ions and electrons was described by projector augmented wave (PAW) and generalized gradient approximation (GGA) with Perdew-Burke-Ernzerhof (PBE) functional [S17,S18]. The kinetic cut-off energy for the plane-wave basis set was 400 eV. The Brillouin zone integration was sampled with 3 × 3 × 1 Monkhorst-Pack grid. All the atoms were fully relaxed until the Hellmann-Feynman force on each atom was less than –0.02 eV $Å^{-1}$ and 10^{-5} eV. Here, we investigated the (003), (012), (104) and (110) planes of Bi with the supercell of 3 × 4 × 1 unit cells, where 6 atomic layers with the bottom 2 atomic layers were fixed along the z direction and another 15 Å vacuum space was included to avoid the periodic interaction along the y and z direction, respectively.

2. Supplementary figures

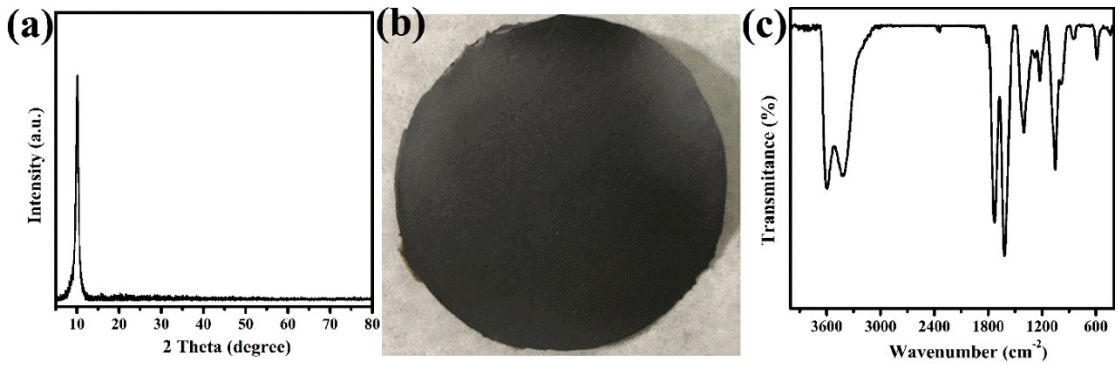

Fig. S1 (a) PXRD pattern, (b) photographic picture, and (c) IR spectrum of the GO paper.

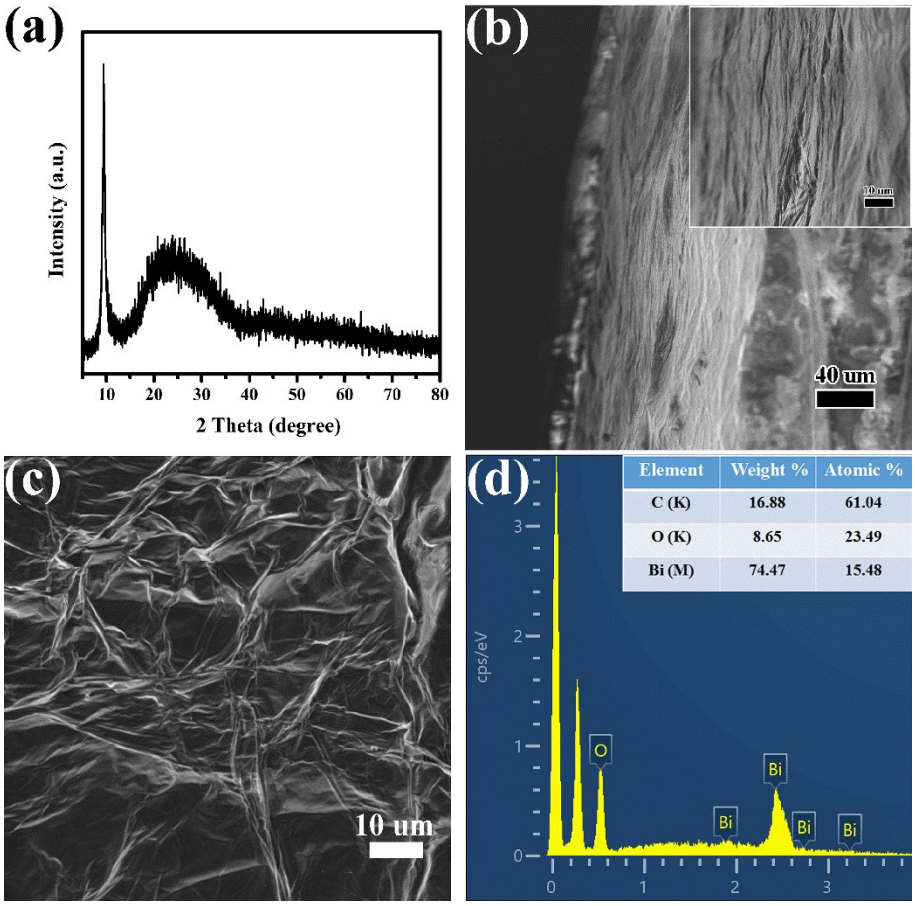

Fig. S2 (a) PXRD pattern, (b,c) plan view and cross-sectional view of the SEM images, and (d) EDX spectrum of the GO paper adsorbed with $Bi(NO_3)_3$.

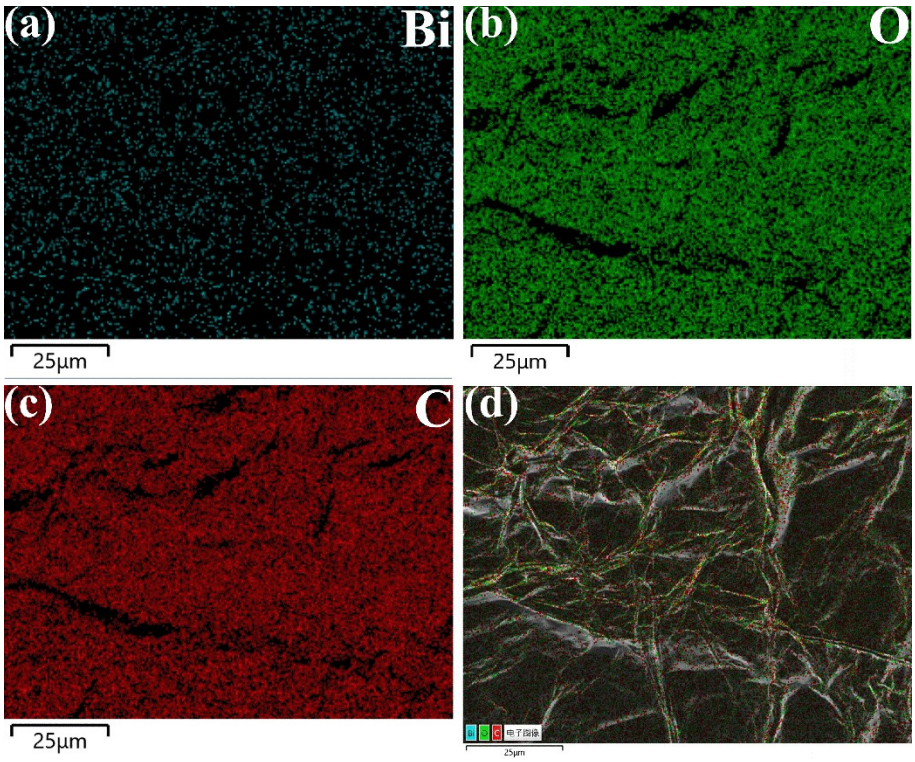

Fig. S3 EDX element mapping images of the GO paper adsorbed with $Bi(NO_3)_3$.

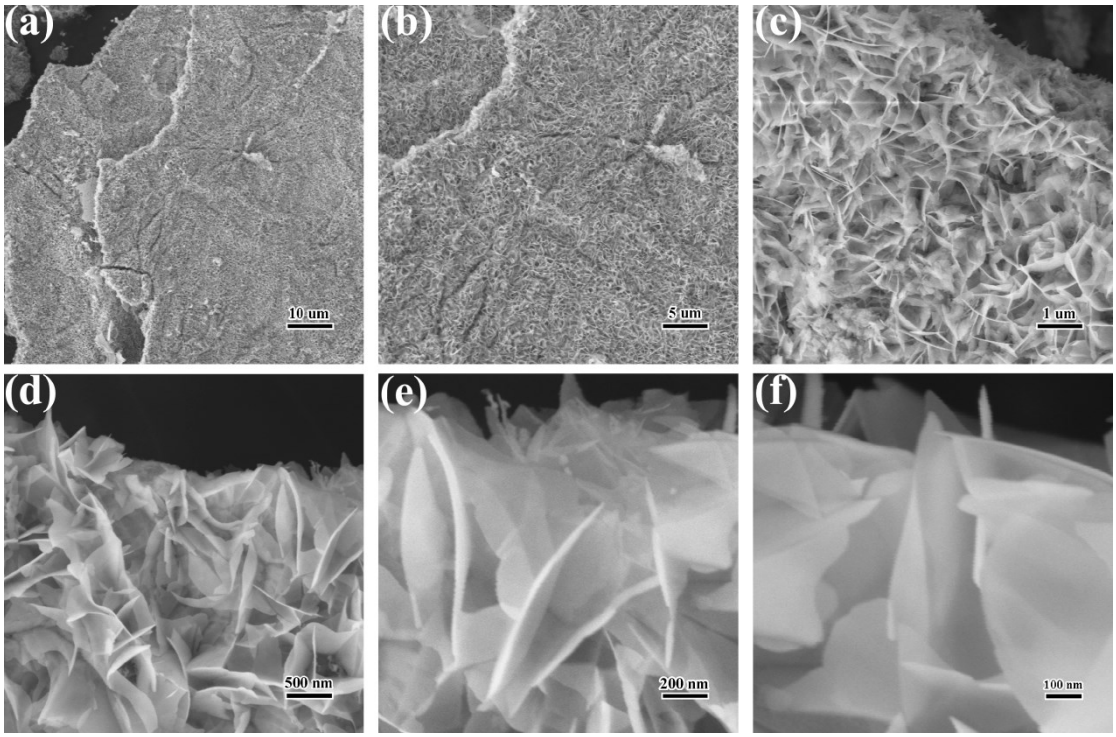

Fig. S4 SEM images of Bi_2O_3-NS-NW composed of the interconnected Bi_2O_3 NSs.

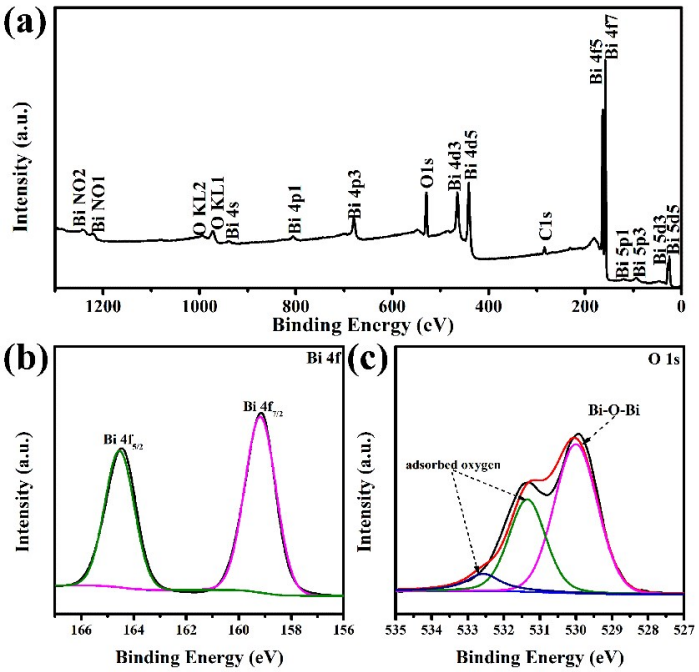

Fig. S5 XPS spectra of Bi_2O_3-NS-NW: (a) survey spectrum, high-resolution (b) Bi 4f and (c) O 1s spectra.

XPS survey spectrum of Bi_2O_3-NS-NW shows different orbital peaks of Bi, O and C elements. The banding energies obtained in the XPS analysis were corrected using the C 1s peak (284.8 eV) as reference originated from carbon binder. The high-resolution XPS spectrum of Bi_2O_3-NS-NW presents spin–orbit split doublets of Bi 4f with the peaks at 164.2 and 158.9 eV, corresponding to Bi $4f_{5/2}$ and Bi $4f_{7/2}$. Additionally, the O 1s spectrum exhibits a peak at 530.3 eV that corresponds to the oxygen in metal oxide, further confirming the formation of Bi_2O_3.

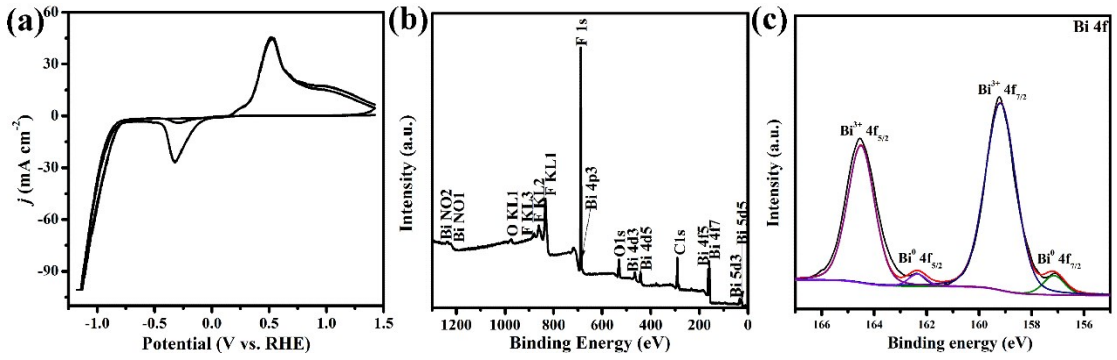

Fig. S6 (a) CV curve of Bi_2O_3-NS-NW in CO_2-saturated 0.5 M $KHCO_3$; (b, c) XPS survey spectrum and Bi 4f spectrum of Bi-ene-NW.

Fig. S6a depicts the cyclic voltammetry (CV) curve of Bi_2O_3-NS-NW in CO_2-saturated 0.5 M $KHCO_3$, which exhibits a pronounced cathodic wave peaked at −0.35 V and sequential anodic waves between 0.2 and 1.2 V. They correspond to the redox interconversion between Bi^{3+} and metallic Bi. XPS survey spectrum of Bi-ene-NW in Fig. S6b presents orbital peaks of the Bi, C, F and O elements, and the F element originates from the Nafion polymer. The high-resolution Bi 4f XPS spectrum were fitted and analyzed, as shown in Fig. S6c, which can be deconvoluted into four peaks, corresponding to Bi $4f_{5/2}$ (Bi^{3+} and Bi^0) and Bi $4f_{7/2}$ (Bi^{3+} and Bi^0). The appearance of trivalent bismuth in Bi-ene-NW should be attributed to partial oxidation of its highly exposed surface.

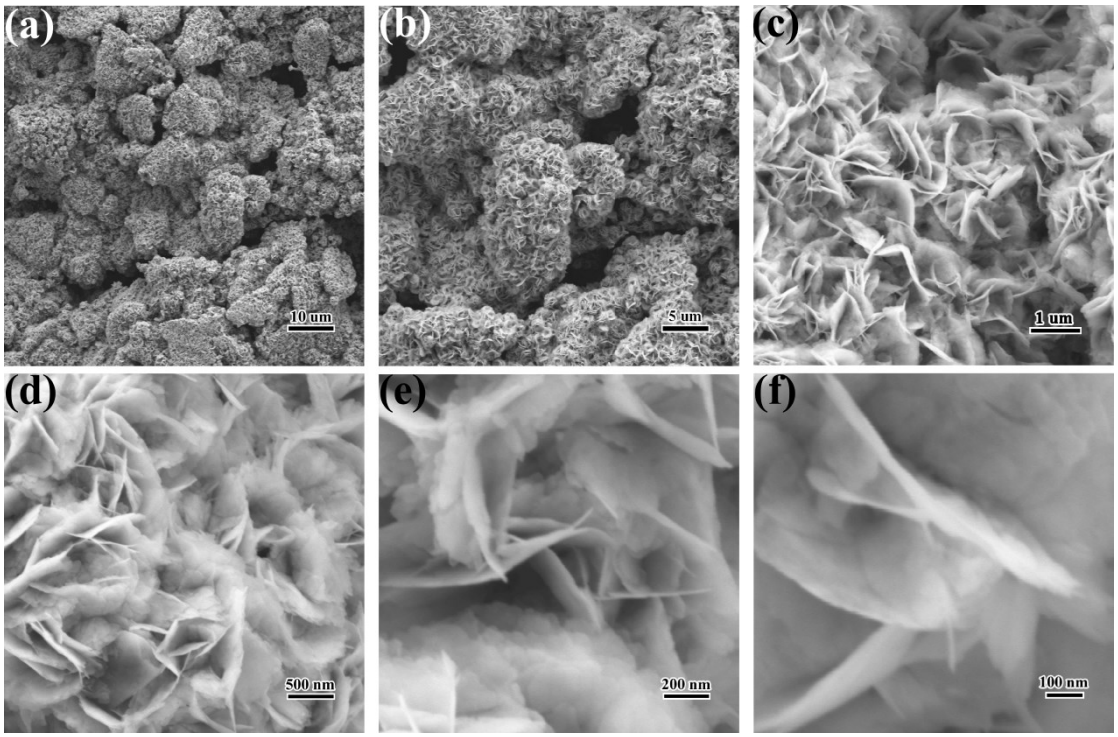

Fig. S7 SEM images of Bi-ene-NW at different magnifications.

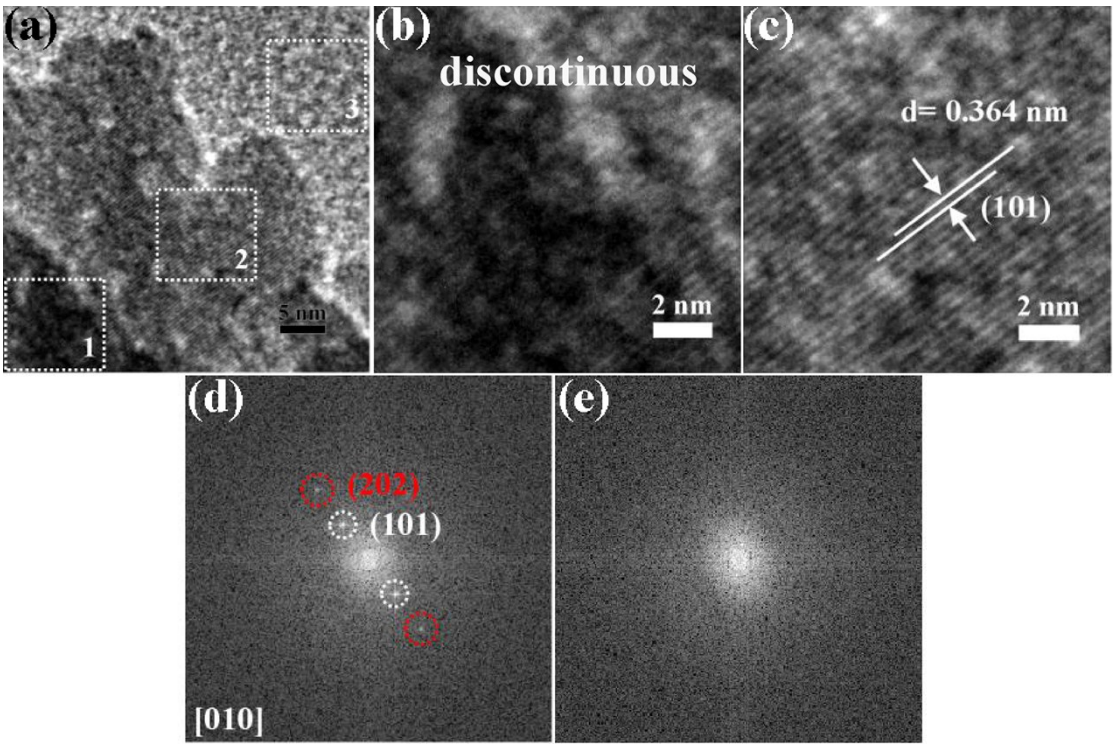

Fig. S8 HRTEM images and FFT patterns of Bi-ene-NW: (a-b) HRTEM images with the enlarged (b) region 1 and (c) region 2; FFT patterns of (d) region 2 and (e) region 3.

Fig. S8a shows that the HRTEM image of Bi-ene-NW with three highlighted regions. The noticeable discontinuous lattice fringes were observed (Fig. S8b), which may be pertained to the inherited lattice defects. The lattice fringes of 0.364 nm are assigned to the (101) planes of rhombohedral Bi (Fig. S8c). The FFT pattern of region 2 can be assigned to the (101) and (202) facets (Fig. S8d). The FFT pattern of region 3 presents its amorphous characteristic, which may result from partial oxidation of Bi (Fig. S8e).

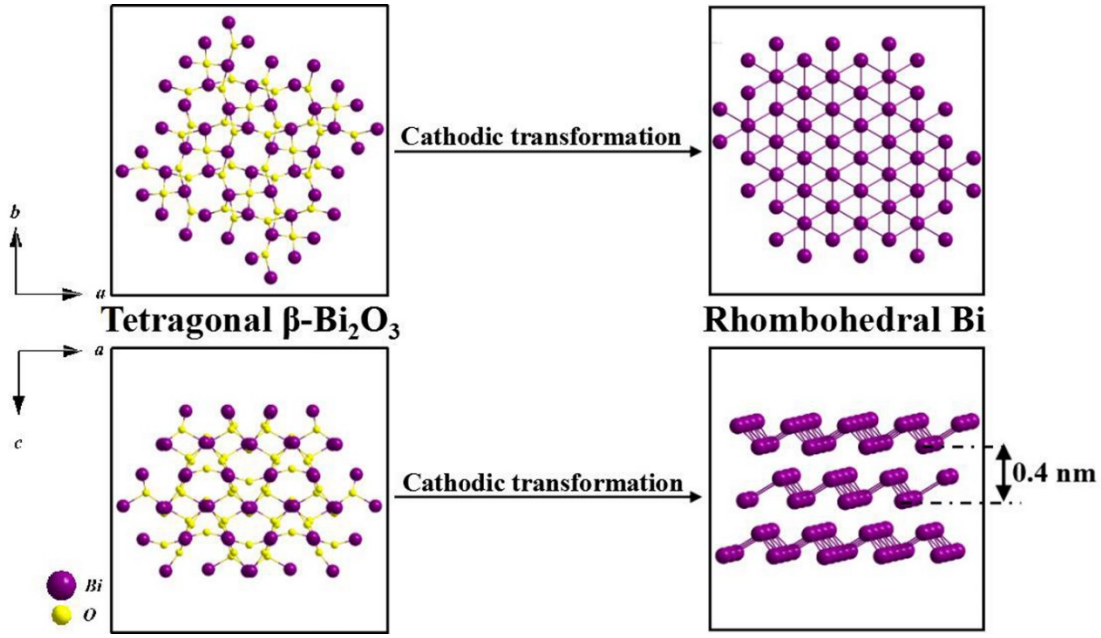

Fig. S9 The crystal structure evolution of tetragonal β-Bi_2O_3 to rhombohedral Bi upon the cathodic transformation.

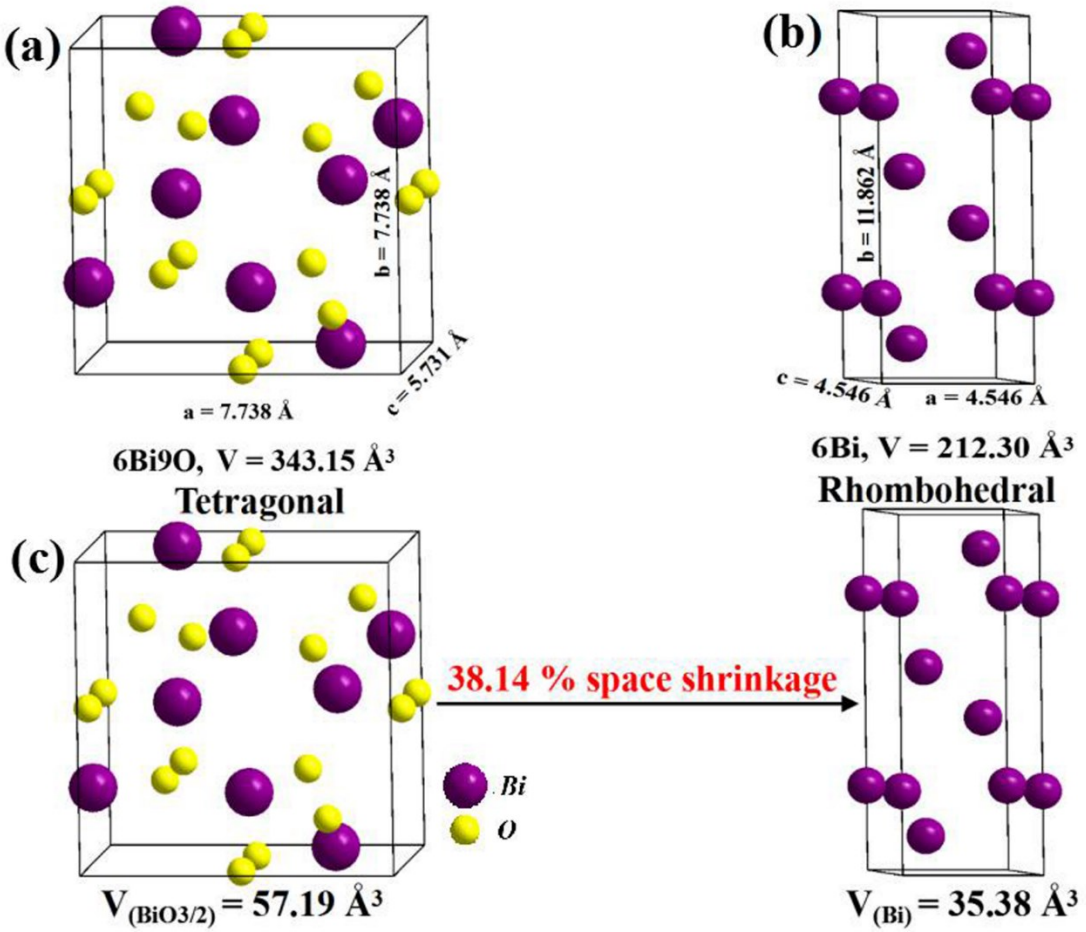

Fig. S10 Theoretical investigation of the space shrinkage from tetragonal β-Bi_2O_3 to rhombohedral Bi upon the cathodic transformation: (a, b) Unit cell parameters of Bi_2O_3 and Bi; (c) Volumes normalized to Bi atoms and space shrinkage upon the transformation of Bi_2O_3 to metallic Bi.

Fig. S10 shows the unit cell parameters of β-Bi_2O_3 and Bi. The cell volumes of Bi_2O_3 and Bi are 343.15 (containing 6 Bi and 9 O atoms) and 212.3 $Å^3$ (containing 6 Bi atoms), respectively, where their volumes normalized to Bi atoms are calculated to be 57.19 and 35.38 $Å^3$, respectively. Correspondingly, the space shrinkage upon the transformation of Bi_2O_3 to metallic Bi should be 38.14%.

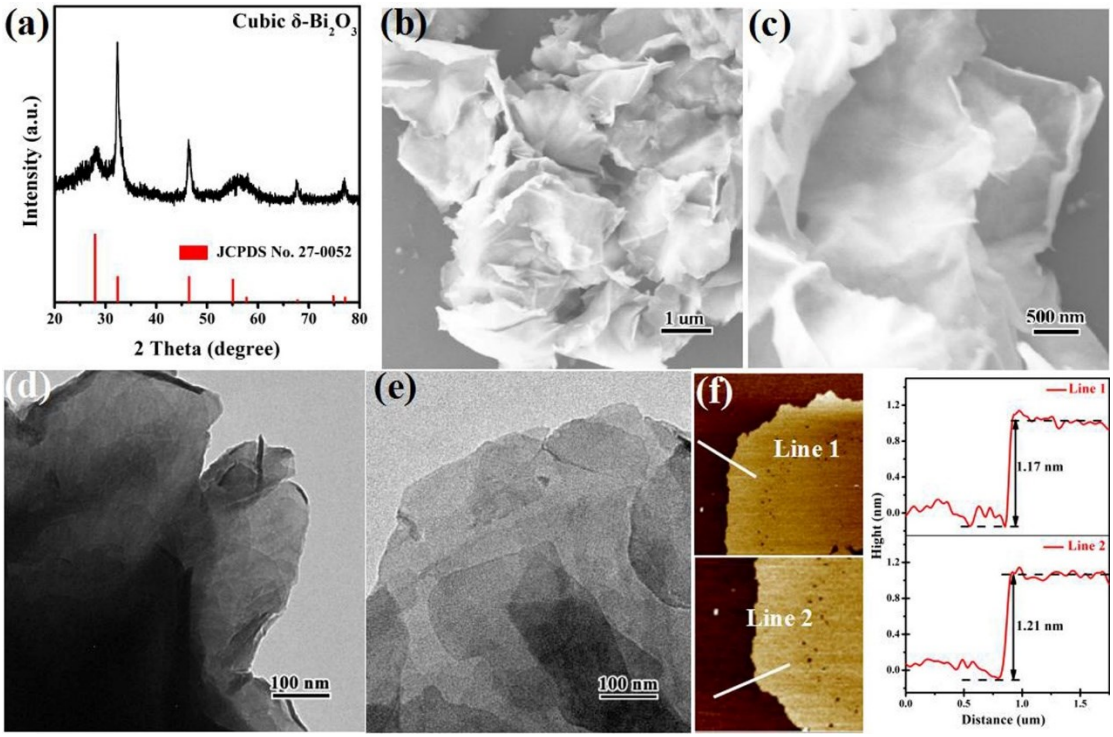

Fig. S11 Characterization of the Bi_2O_3 NSs as the precursor of Bi-NFs: (a) PXRD; (b, c) SEM images; (d, e) TEM images; (f) AFM images and corresponding height profiles.

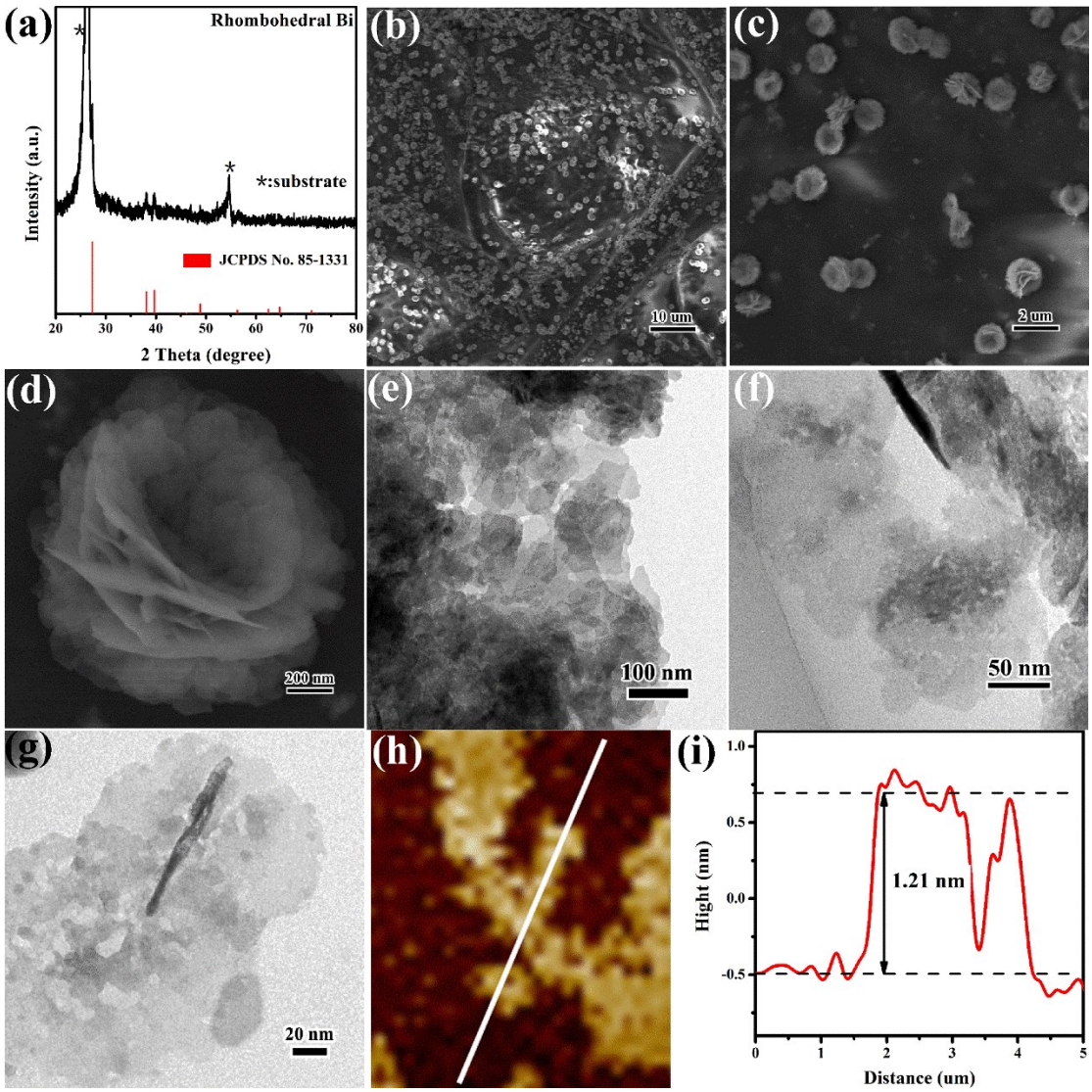

Fig. S12 Characterization of Bi-NFs: (a) PXRD; (b-d) SEM images at different magnifications; (e-g) TEM images; (h, i) AFM images and corresponding height profiles.

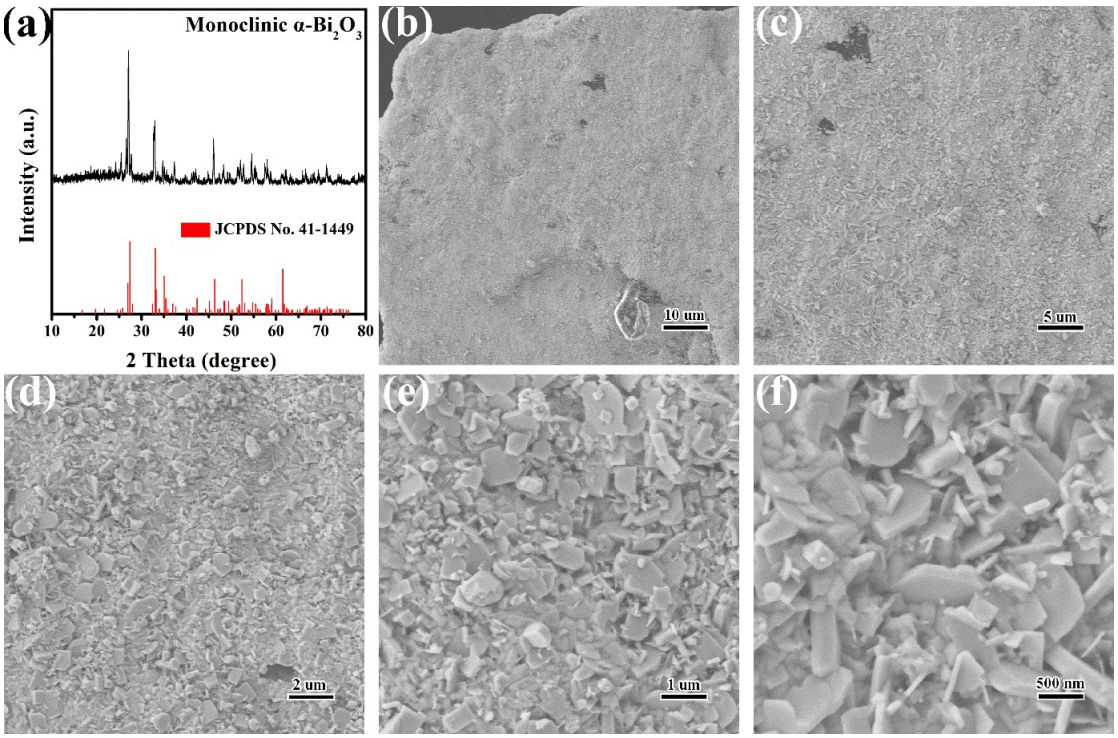

Fig. S13 Characterization of the oxidized commercial Bi powder as the precursor of Bi-MPs: (a) PXRD pattern; (b-f) SEM images at different magnifications.

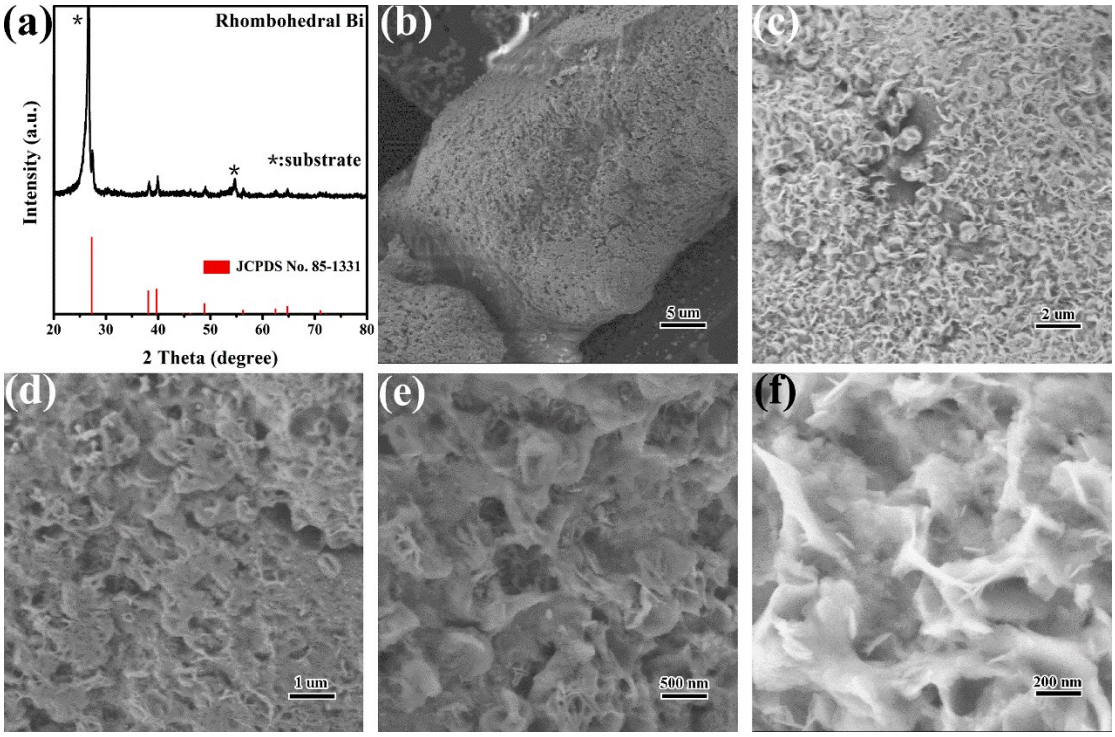

Fig. S14 Characterization of Bi-MPs: (a) PXRD pattern; (b-f) SEM images at different magnifications.

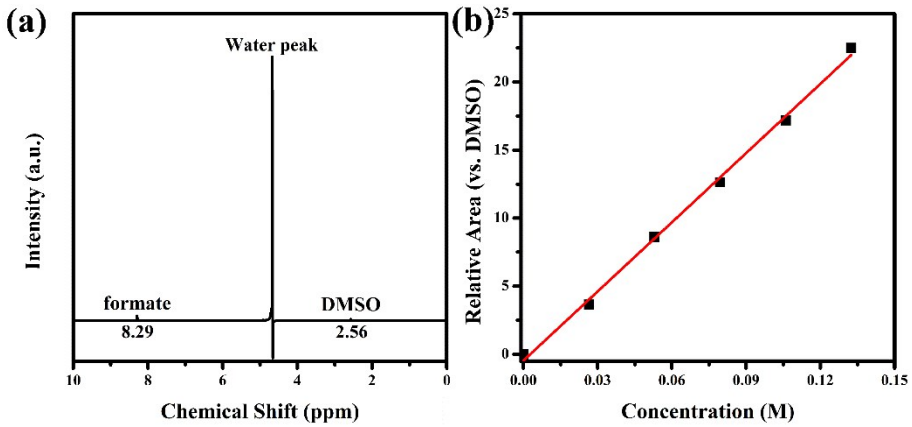

Fig. S15 Identification and quantification of formate by NMR: (a) A typical NMR spectrum of the recycled electrolyte containing formate after electrolysis; (b) Standard curve by plotting the formate concentration with respect to the NMR peak area ratio of formate/DMSO.

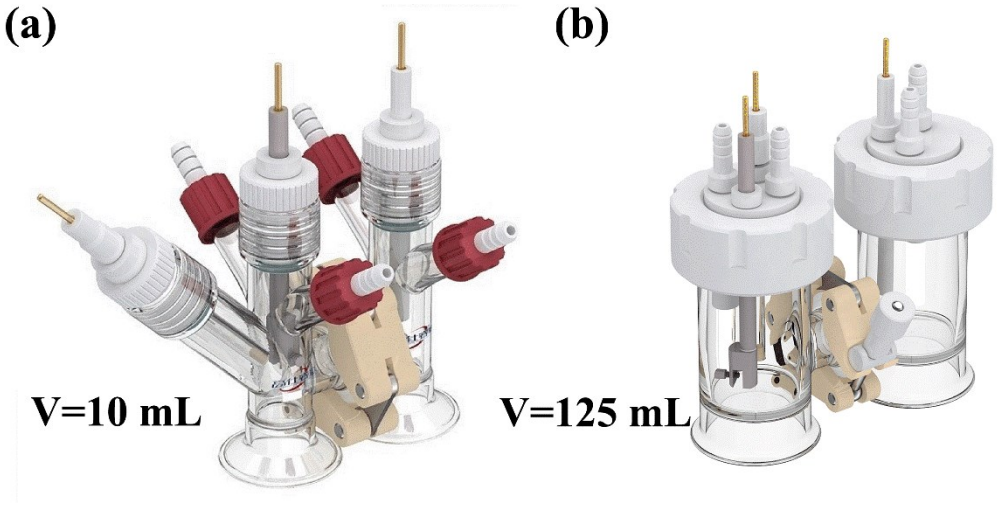

Fig. S16 Photographic images of two typical H-type cells with different volumes for electrocatalytic CO_2 reduction.

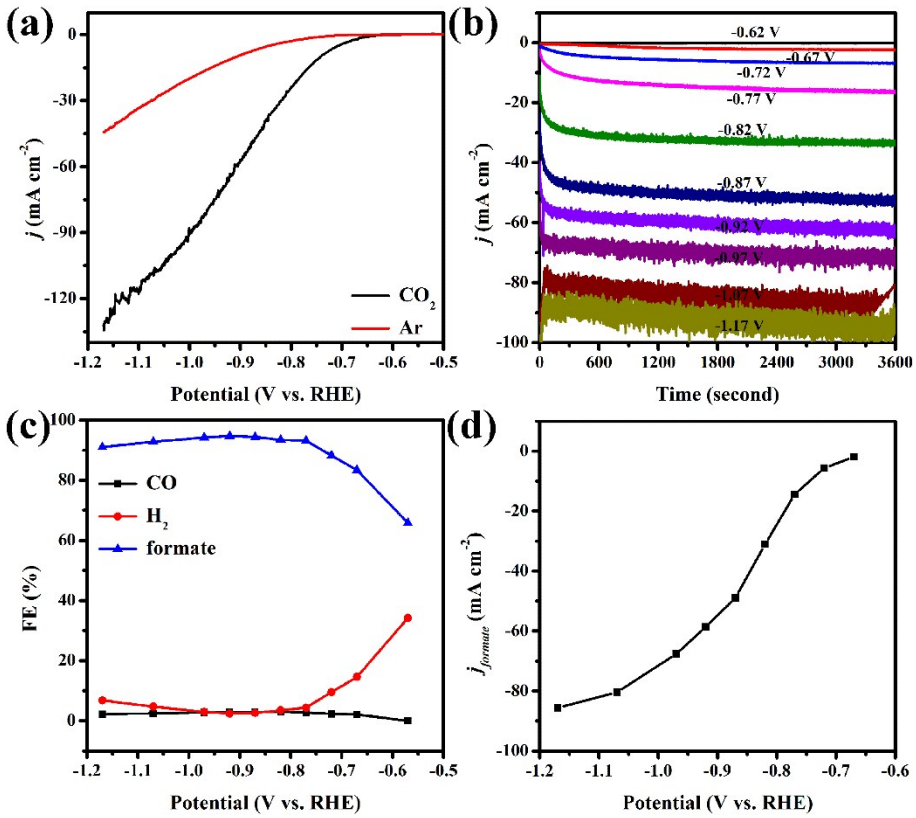

Fig. S17 Electrocatalytic CO_2RR performance of Bi-ene-NW in CO_2-saturated 0.5 M $KHCO_3$: (a) Polarization curves in Ar- or CO_2-saturated solution; (b) Total current densities at designated potentials; (c) FE for formate, CO and H_2; (d) Partial current densities of formate.

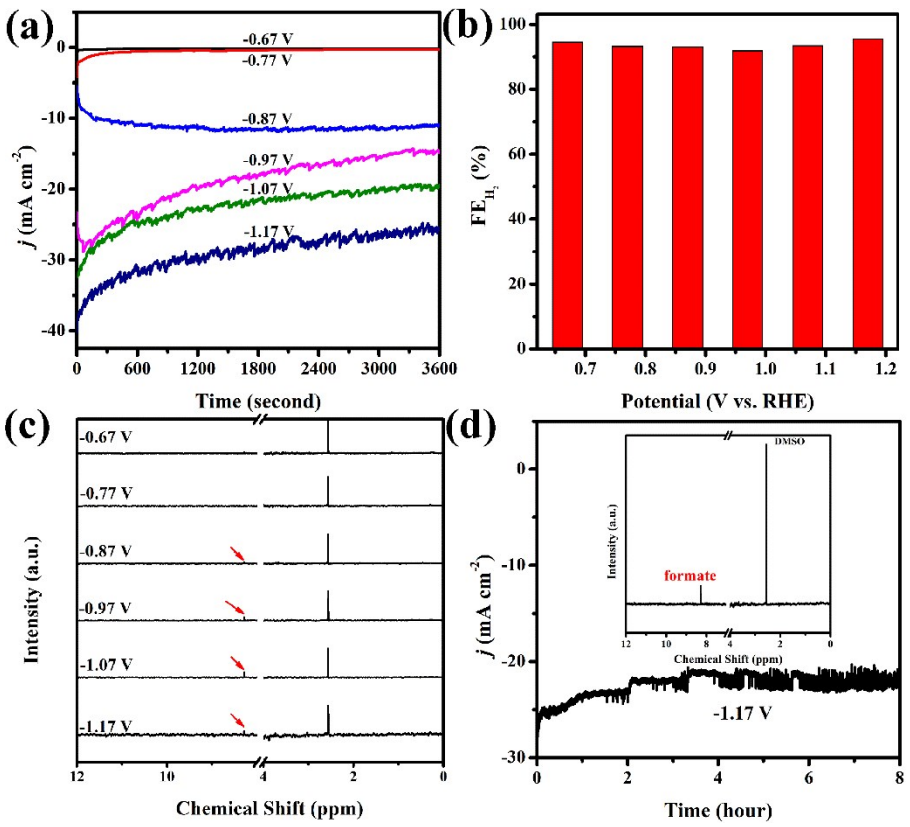

Fig. S18 Electrocatalytic performance of Bi-ene-NW in Ar-saturated 0.5 M $KHCO_3$: (a) Total current densities at designated potentials; (b) FE for H_2; (c) NMR spectra of the catholyte recycled after electrolysis at designated potentials; (d) The long-term electrolysis at –1.17 V.

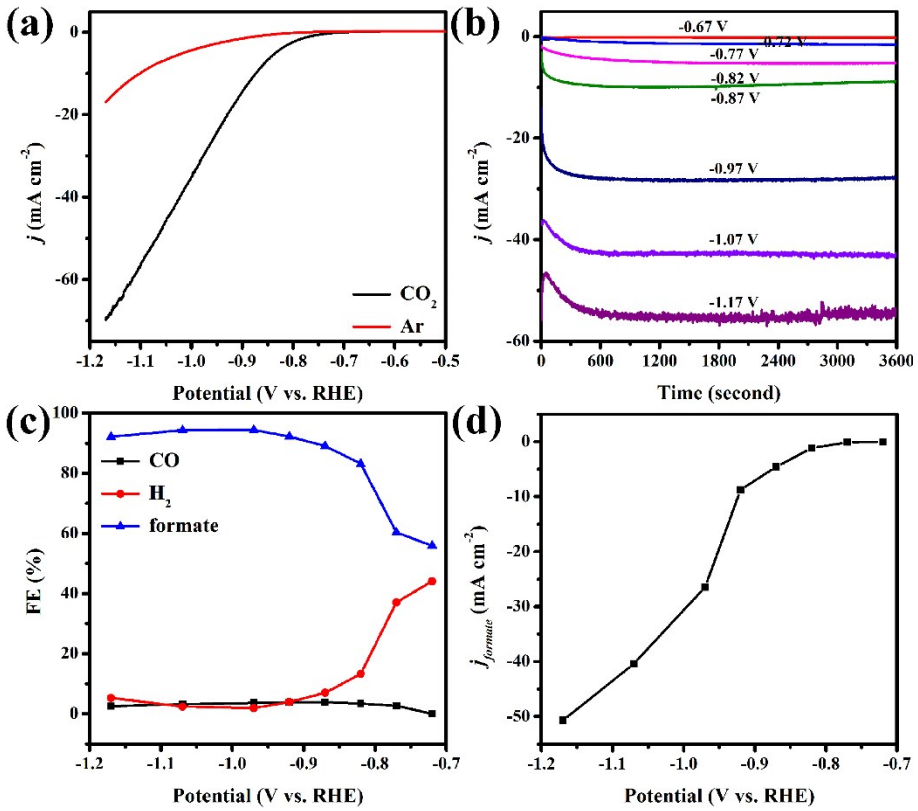

Fig. S19 Electrocatalytic CO_2RR performance of Bi-NFs in CO_2-saturated 0.5 M $KHCO_3$: (a) Polarization curves; (b) Total current densities at designated potentials; (c) FE for formate, CO and H_2; (d) Partial current densities of formate.

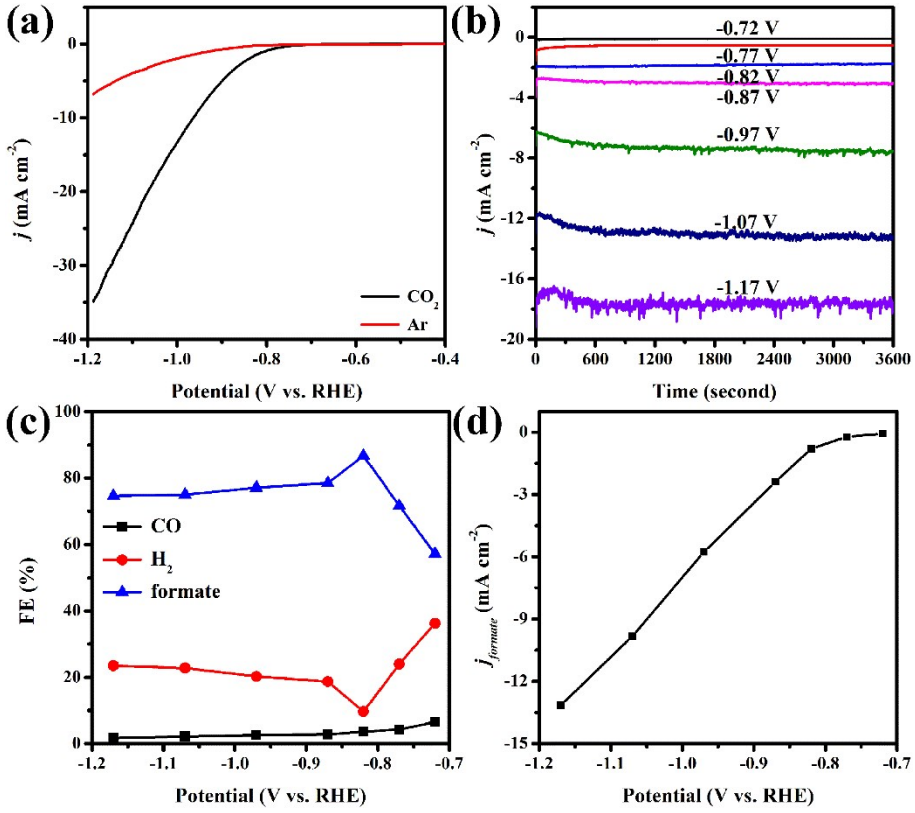

Fig. S20 Electrocatalytic CO_2RR performance of Bi-MPs in CO_2-saturated 0.5 M $KHCO_3$: (a) Polarization curves; (b) Total current densities at designated potentials; (c) FE for formate, CO and H_2; (d) Partial current densities of formate.

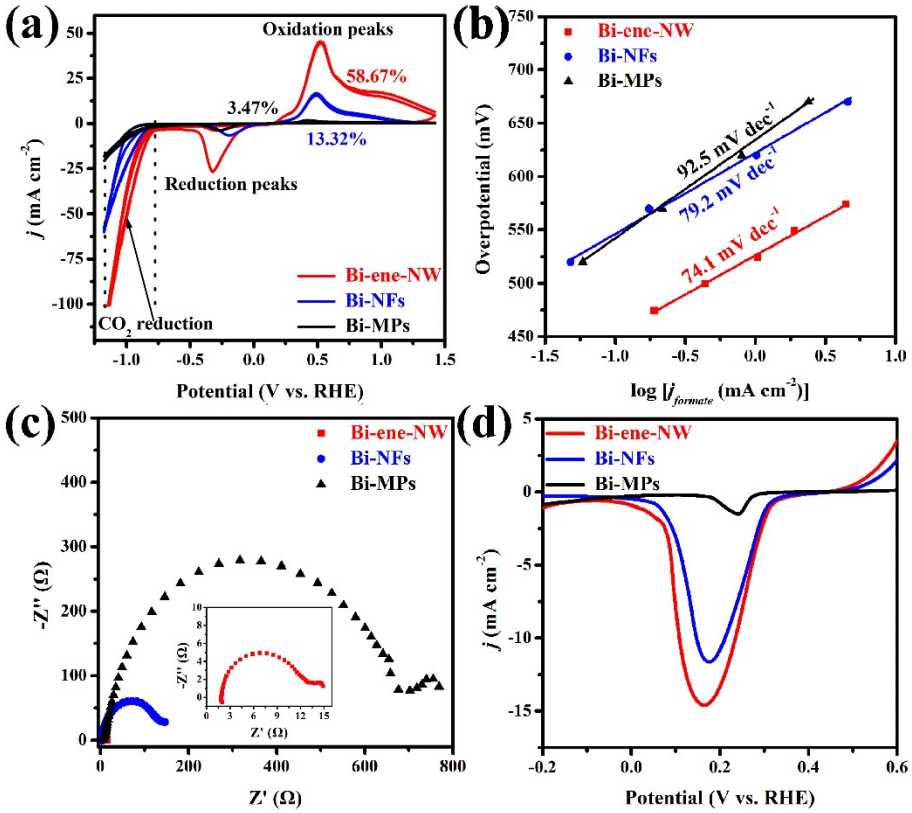

Fig. S21 Different Bi-based catalysts for electrocatalytic CO_2 reduction: (a) CV curves; (b) Tafel plots; (c) Nyquist plots; (d) LSV curves in Ar-saturated 0.1 M KOH electrolyte.

CV curves of Bi-ene-NW, Bi-NFs and Bi-MPs electrode in a potential range from −1.17 to 1.43 V are shown in Fig. S21a at a scan rate of 100 mV s^{-1}. The oxidation peak at 0.525 V over Bi-ene-NW belongs to the coversion of metallic Bi to Bi^{3+}, the oxidation peak at −0.325 V belongs to the coversion of Bi^{3+} to metallic Bi, and the negative peak between of -1.17 and -0.65 V is attributed to CO_2 reduction. Based on the oxidation peak, the percentage (χ) of active Bi sites to the total Bi sites can be calculated as follows:

$$\chi = S_{op} / (n_{total} \times N \times v \times F \times S_{area}) \times 100\% \quad (4)$$

where S_{Op} is area of oxidation peak, n_{total} is the total Bi sites which refers to the molar amount of Bi based on Bi_2O_3 loaded to the electrode, N is the number of electrons required to convert Bi to Bi^{3+}, v is scan rate, F is Faraday constant (96 485 C mol^{-1}), S_{area} is the area of electrode.

Generally, a slope of 118 mV dec^{-1} implies the RDS is the formation of $CO_2{}^{*-}$, whereas a slope of 59 mV dec^{-1} signifies that the subsequent slower step after $CO_2{}^{*-}$ formation is the RDS. For Bi-ene-NW, Tafel slope of 75 mV dec^{-1} is very close to 59 mV dec^{-1}.

The quick-balanced CO_2^{*-} enables protonation to proceed spontaneously to form the adsorbed $OCHO^*$ for boosting the CO_2RR via the proton-coupled electron transfer (Fig. S21b). The electrochemical impedance spectroscopy (EIS) was recorded at –0.66 V *vs*. RHE with the frequency ranging from 0.1 to 10^5 Hz at the AC amplitude of 5 mV (Fig. S21c). The adsorption of intermediates on active sites is very key for the reduction of CO_2. The overpotential of hydroxyl adsorption is considered a measure of binding strength of intermediates on catalytic surface, and the smaller overpotential indicates the larger binding energy (stronger binding) of intermediates. Due to the similar binding behaviors, the adsorption of OH^- as a surrogate of CO_2^{*-} was examined through a cathodic LSV scan between −0.2 and 0.6 V in Ar-saturated aqueous 0.1 M KOH solution at a scan rate of 20 mV s^{-1} (Fig. S21d).

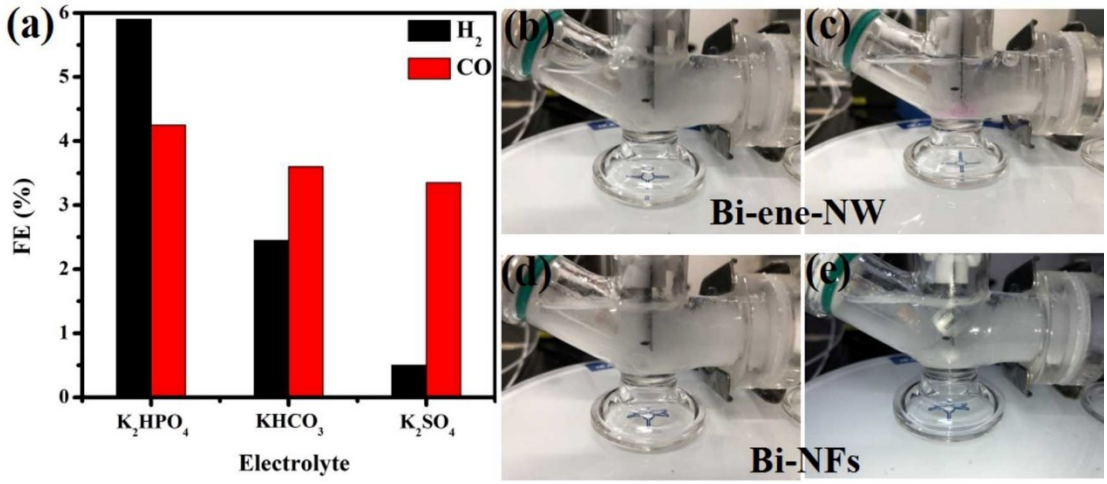

Fig. S22 (a) The pH-dependent FE of H_2 and CO over Bi-ene-NW in different electrolytes (0.5 M); (b-e) Photographic images of the phenolphthalein color transition experiment over Bi-ene-NW and Bi-NFs conducted at –1.0 V *vs.* RHE in CO_2-saturated aqueous 0.5 M $KHCO_3$ solution before (left) and after (right) electrolysis for 1 min.

In the local pH effect experiment, CO_2-saturated 0.5 M K_2HPO_4, $KHCO_3$ and K_2SO_4 were used as the respective electrolytes, and the geometric current density was set as a constant value of 20 mA cm^{-2} (Fig. S22a). The phenolphthalein color transition experiment was conducted at –1.0 V *vs.* RHE and 1 mL of 0.05 M phenolphthalein in ethanol was added into the electrolyte (CO_2-saturated aqueous 0.5 M $KHCO_3$ solution) in the working compartment (Fig. S22b-e). Fig. S22b,d shows that at the beginning of the experiment, no pink color was seen in both electrolytes using Bi-ene-NW and Bi-NFs as the catalysts (The pH value of CO2-saturated aqueous 0.5 M KHCO3 solution is about 7.4, while the colorless-to-pink transition point of phenolphthalein is at pH ~ 8.3). After electrolysis for 1 min, dark pink color could be observed around the Bi-ene-NW cathode, while pink color was still unseen in the Bi-NFs cathode (Fig. S22c,e). The results illustrate that the higher current density over Bi-ene-NW could enhance the local pH over 8.3, while the increase of local pH over Bi-NFs was too small to trigger the phenolphthalein color transition.

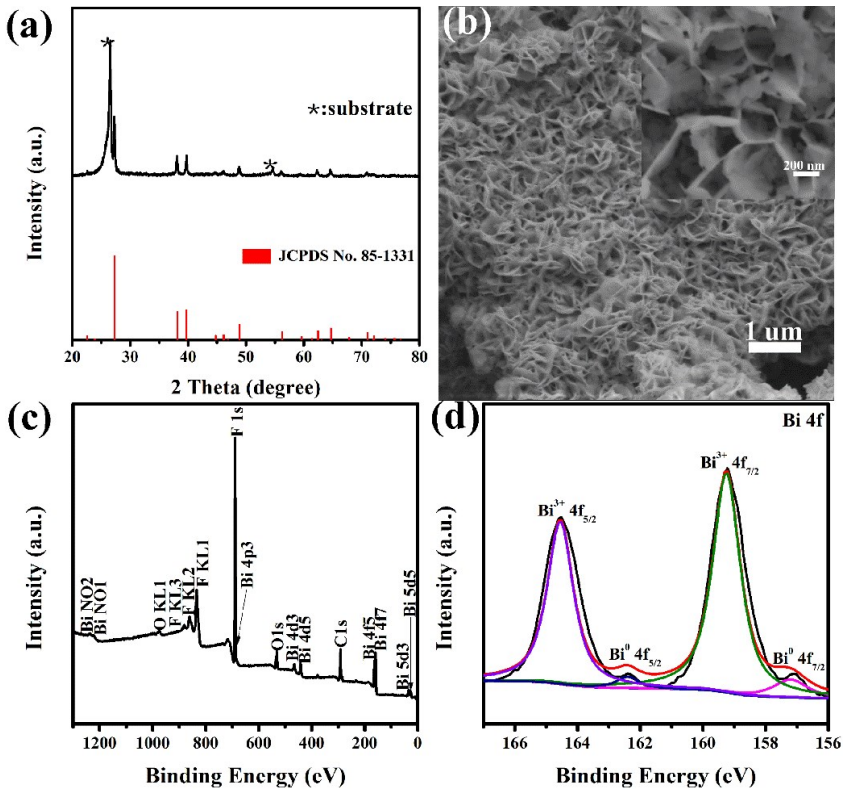

Fig. S23 Characterization of Bi-ene-NW after long-term stability test: (a) PXRD pattern; (b) SEM images; (c) XPS survey spectrum; (d) XPS Bi 4f spectrum.

The crystalline state, morphology and surface condition of the recycled Bi-ene-NW also were surveyed by PXRD, SEM and XPS measurements. No obvious change in crystalline state, and morphology for the recycled Bi-ene-NW was observed in Fig. S23 (a, b). XPS survey spectrum in Fig. S23c presents the orbital peaks of the Bi, C, F and O elements, and the F element originates from the Nafion polymer. The appearance of Bi^{3+} in Bi-ene-NW should be attributed to partial oxidation of its highly exposed surface (Fig. S23d).

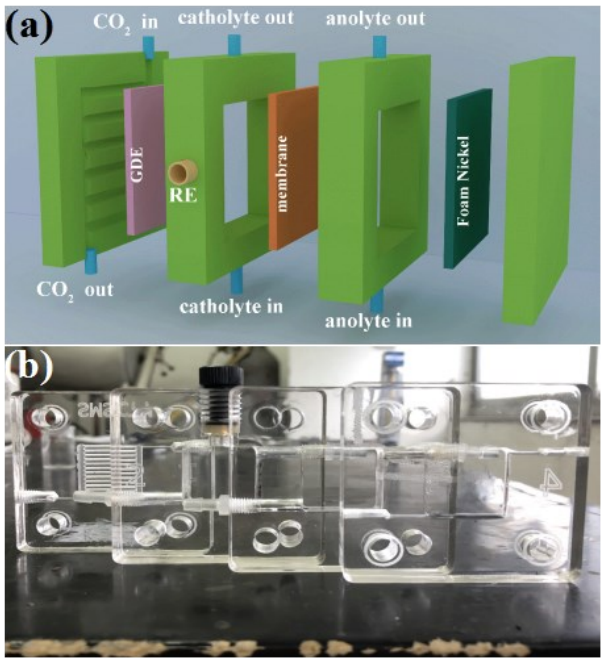

Fig. S24 Flow cell configuration for electrocatalytic CO_2 reduction: (a) schematic diagram; (b) actual photograph.

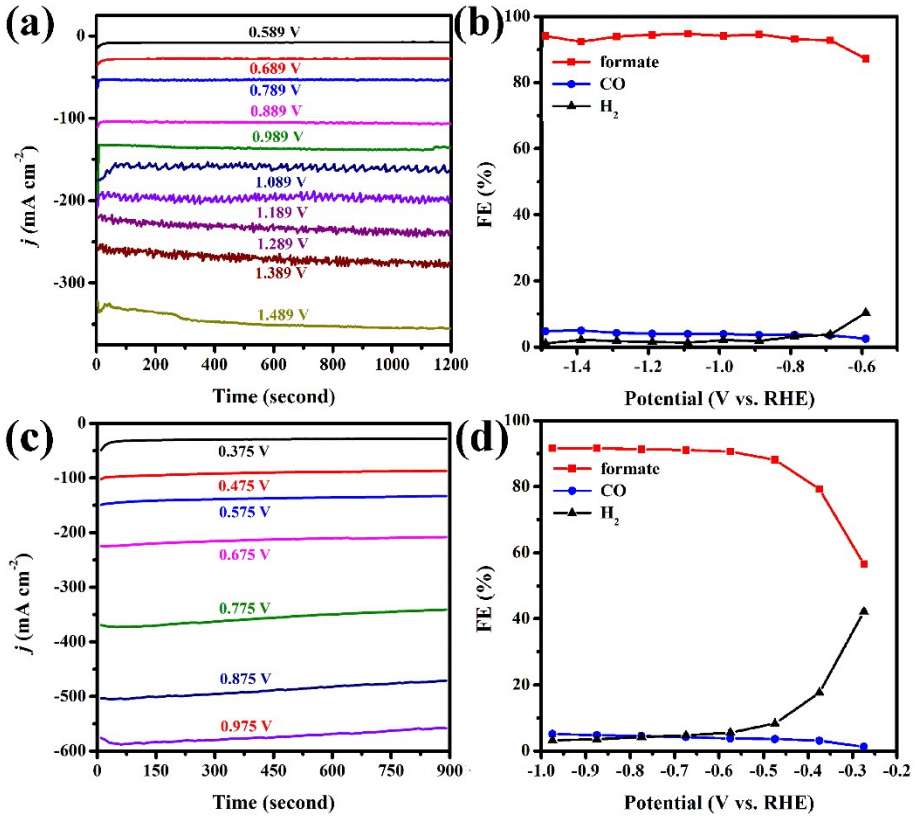

Fig. S25 Electrocatalytic CO_2RR performance of Bi-ene-NW in a flow cell: Chronoamperometric responses at different potentials and corresponding FE for formate, CO and H_2 in (a, b) 1.0 M $KHCO_3$ and (c, d) 1.0 M KOH.

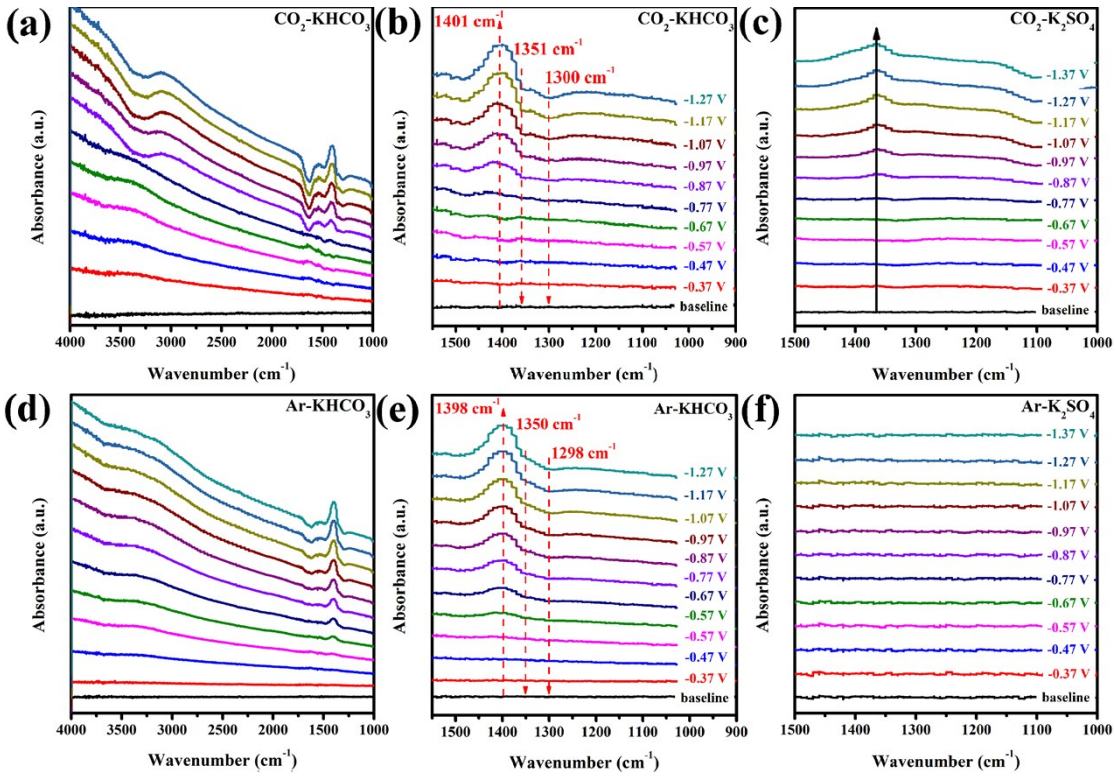

Fig. S26 Operando ATR-IR spectra collected over Bi-ene-NW at different applied potentials in (a, b) CO_2-saturated 0.5 M $KHCO_3$; (c) CO_2-saturated 0.5 M K_2SO_4; (d, e) Ar-saturated 0.5 M $KHCO_3$; and (f) Ar-saturated 0.5 M K_2SO_4.

The operando ATR-IR spectra were collected in a single electrochemical cell by using a typical three-electrode system (Bi-ene-NW, Pt wire and saturated Ag/AgCl were used as the working, counter and reference electrodes). During the test process, the surface of the working electrode was pressed close to a Ge single crystal to ensure the obtaining of better IR signals.

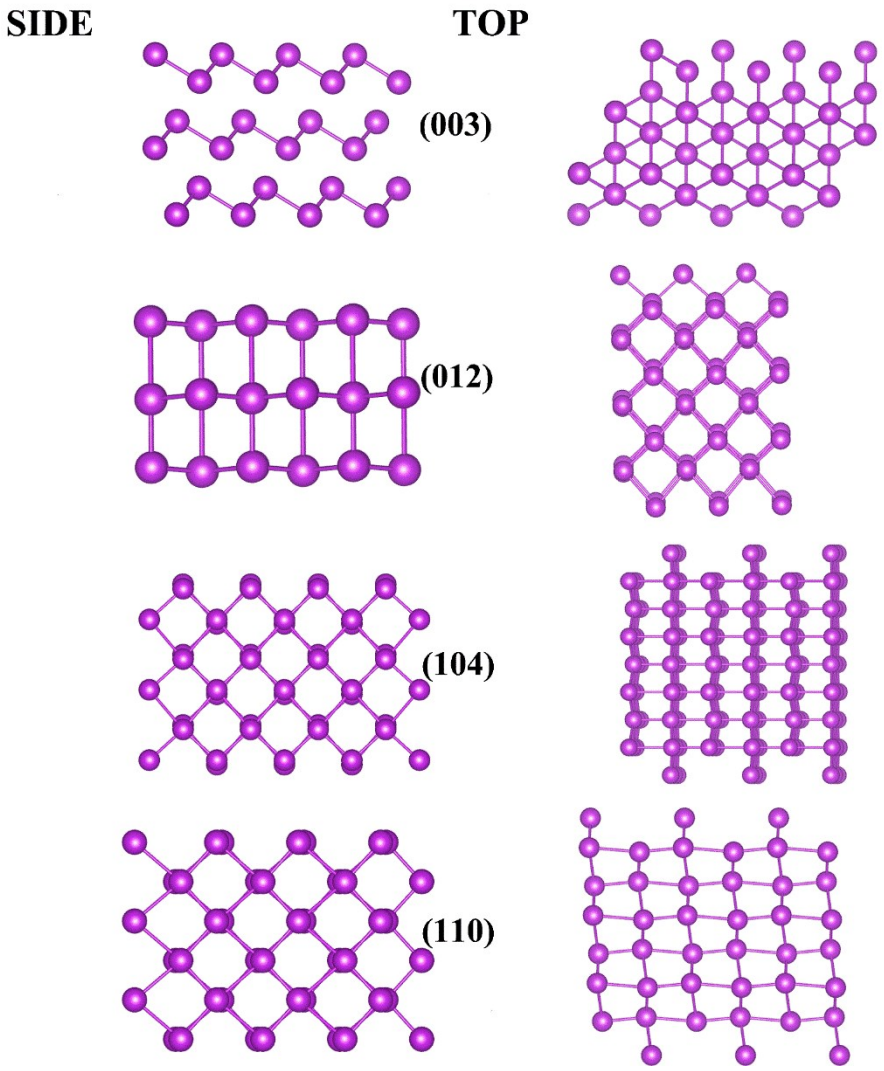

Fig. S27 Diagram of different crystal planes of Bi-ene-NW.

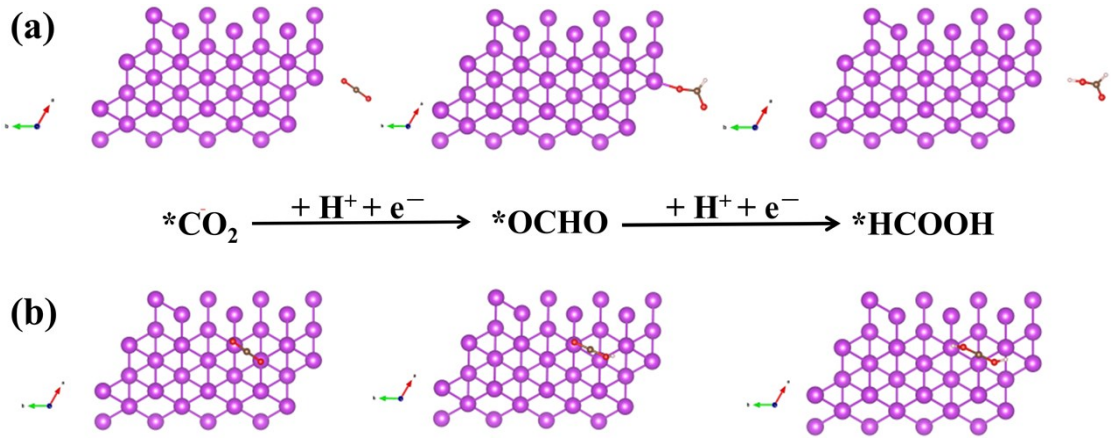

Fig. S28 The DFT–optimized intermediate species along the reaction pathways for CO_2 electroreduction to formate on the (a) edge and (b) plane of Bi-ene.

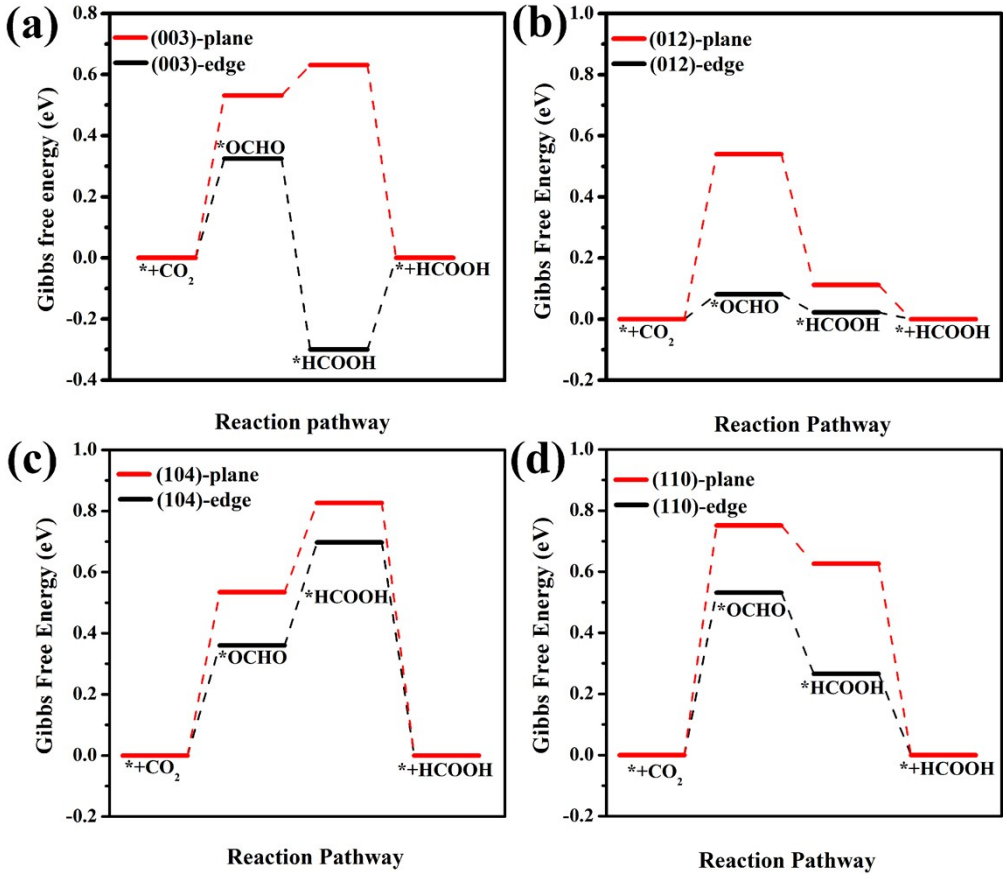

Fig. S29 DFT-calculated ΔG in the reaction pathways of CO_2 conversion into formate on the plane site and edge site: (a) (003) plane; (b) (012) plane; (c) (104) plane; (d) (110) plane.

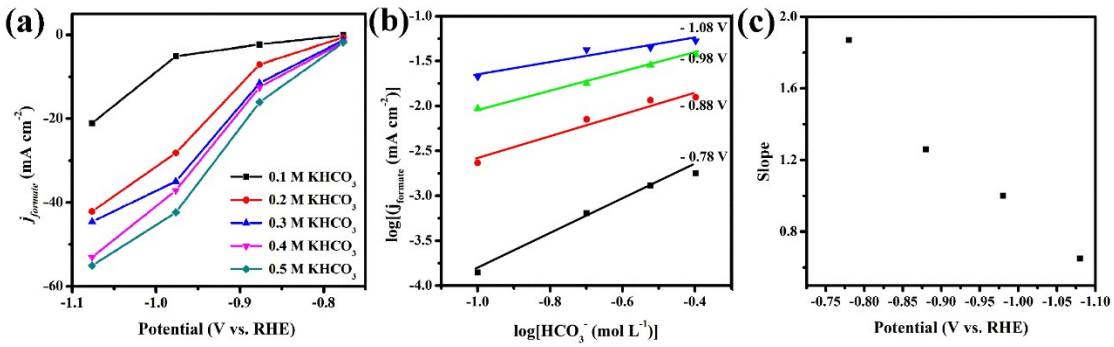

Fig. S30 (a) Partial current densities of formate over Bi-ene-NW in CO_2-saturated $KHCO_3$ solution with different concentrations; (b) Plots of log[$j_{formate}$ (mA cm^{-2})] versus log[HCO_3^- (mol L^{-1})] at different constant potentials; (c) The corresponding slopes of the plots in (b) at different potentials.

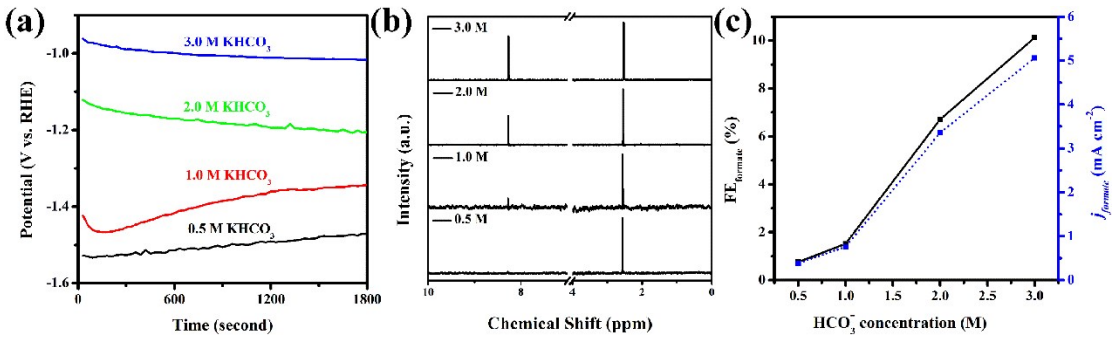

Fig. S31 Electrocatalytic performance of Bi-ene-NW in Ar-saturated $KHCO_3$ with different HCO_3^- concentrations: (a) Chronoamperometric responses at the same current density of 50 mA cm^{-2}; (b) The NMR spectra of the catholytes recycled after electrolysis for 0.5 h; (c) $FE_{formate}$ and partial current densities of formate at 50 mA cm^{-2}.

3. Supplementary tables

Table S1 CO_2RR catalytic performances of recently reported Bi-based catalysts for formate production in H-cell.

Catalyst	Electrolyte	Potential (V vs. RHE)	Current density (mA cm^{-2})	FE (%)	Stability	Reference
Bi-ene-NW	**0.5 M $KHCO_3$**	**−1.17**	**88**	**92**	**500 h (~100 mA)**	**This work**
Bi nanosheet	0.1 M $KHCO_3$	−1.2	18	70	10 h (~17 mA)	S1
BOCNS	0.5 M $NaHCO_3$	−1.0	35	83	12 h (~11 mA)	S2
AgBi-500	0.1 M $KHCO_3$	−1.1	26	85	12 h (~13 mA)	S3
mpBi	0.5 M $NaHCO_3$	−1.0	17	87	12 h (~5 mA)	S4
Cufoam@BiNW	0.5 M $NaHCO_3$	−1.09	46	88	12 h (~16 mA)	S5
NTD-Bi	0.5 M $KHCO_3$	−1.05	60	90	48 h (~36 mA)	S6
BBNs	0.5 M $NaHCO_3$	−0.85	13.5	91	12 h (~11.5 mA)	S7
Bi-Sn/CF	0.5 M $KHCO_3$	−1.14	53	96	100 h (~55 mA)	S8

Table S2 CO_2RR catalytic performances of recently reported Bi-based catalysts for formate in Flow-cell.

Catalyst	Electrolyte	Potential (V vs. RHE)	Current density (mA cm^{-2})	FE (%)	Stability	Reference
Bi-ene-NW	**1 M $KHCO_3$**	**−1.47**	**350**	**91**	**110 h (~200 mA)**	**This work**
	1 M KOH	**−0.97**	**570**	**91**	**18 h (~200 mA)**	
bismuthene nanosheets	1 M $KHCO_3$	−1.5	325	87	25 h (~50 mA)	S9
Bi_2O_3@C-800	1 M KOH	−1.1	208	93	1 h (~150 mA)	S10
Bi NSs	1 M KOH	−0.465	198	86.55	25 min (~198 mA)	S11
Bi_2S_3 NPs	1 M KOH	−0.59	205	90	6 h (~120 mA)	S12
PD-Bi1	1 M $KHCO_3$	−1.09	46	88	12 h (~16 mA)	S13
	1 M KOH	−0.6	288	98	11 h (~210 mA)	
NTD-Bi	1 M $KHCO_3$	−0.85	140	95	13 h (~140 mA)	S6
	1 M KOH	−0.6	288	98	11 h (~210 mA)	
Leafy Bi-NS	1 M $KHCO_3$	−1.51	400	86.9	10 h (~128 mA)	S14
	1M KOH	−0.67	400	89	10 h (~197 mA)	

4. Supplementary references

S1 W. Zhang, Y. Hu, L. Ma, G. Zhu, P. Zhao, X. Xue, R. Chen, S. Yang, J. Ma, J. Liu and Z. Jin, *Nano Energy*, 2018, **53**, 808-816.

S2 Y. Zhang, X. Zhang, Y. Ling, F. Li, A. M. Bond and J. Zhang, *Angew. Chem. Int. Ed.*, 2018, **57**, 13283-13287.

S3 J. H. Zhou, K. Yuan, L. Zhou, Y. Guo, M. Y. Luo, X. Y. Guo, Q. Y. Meng and Y. W. Zhang, *Angew. Chem. Int. Ed.,* 2019, **131**, 14335-14339.

S4 H. Yang, N. Han, J. Deng, J. Wu, Y. Wang, Y. Hu, P. Ding, Y. Li, Y. Li and J. Lu, *Adv. Energy Mater.*, 2018, **8**, 1801536.

S5 X. Zhang, X. Sun, S.-X. Guo, A. M. Bond and J. Zhang, *Energy Environ. Sci.*, 2019, **12**, 1334-1340.

S6 Q. Gong, P. Ding, M. Xu, X. Zhu, M. Wang, J. Deng, Q. Ma, N. Han, Y. Zhu, J. Lu, Z. Feng, Y. Li, W. Zhou and Y. Li, *Nat. Commun.,* 2019, **10**, 2807.

S7 J. Zhu, J. Fan, T. Cheng, M. Cao, Z. Sun, R. Zhou, L. Huang, D. Wang, Y. Li and Y. Wu, *Nano Energy,* 2020, **75,** 104939.

S8 G. Wen, D. U. Lee, B. Ren, F. M. Hassan, G. Jiang, Z. P. Cano, J. Gostick, E. Croiset, Z. Bai, L. Yang and Z. Chen, *Adv. Energy Mater.,* 2018, **8**, 1802427.

S9 W. Ma, J. Bu, Z. Liu, C. Yan, Y. Yao, N. Chang, H. Zhang, T. Wang and J. Zhang, *Adv. Funct. Mater.*, 2020, **31**, 2006704.

S10 P. Deng, F. Yang, Z. Wang, S. Chen, Y. Zhou, S. Zaman and B. Y. Xia, *Angew. Chem. Int. Ed.,* 2020, **59**, 10807-10813.

S11 X. Wang, W.-J. Yin, Y. Si, X. Wang, X. Guo, W. Guo and Y. Fu, *J. Mater. Chem. A*, 2020, **8**, 19938-19945.

S12 P. Ding, J. Zhang, N. Han, Y. Zhou, L. Jia and Y. Li, *J. Mater. Chem. A*, 2020, **8,** 12385-12390.

S13 Y. Wang, Y. Li, J. Liu, C. Dong, C. Xiao, L. Cheng, H. Jiang, H. Jiang and C. Li. *Angew. Chem. Int. Ed.,* 2021, **60**, 7681-7685.

S14 J. Yang, X. Wang, Y. Qu, X. Wang, H. Huo, Q. Fan, J. Wang, L. M. Yang and Y. Wu, *Adv. Energy Mater.,* 2020, **10**, 2001709.

S15 G. Kresse and J. Hafner*, Phys. Rev. B*, 1993, **47**, 558.

S16 G. Kresse and J. Furthmüller, *Comput. mater. Sci.*, 1996, **6**, 15-50.

S17 P. E. Blöchl, *Phys. rev. B*, 1994, **50**, 17953.

S18 J. P. Perdew, K. Burke and M. Ernzerhof, *Phys. Rev. Lett.,* 1996, **77**, 3865.